Title
Energy response calibration of photon-counting detectors using x-ray fluorescence: a feasibility study

Journal
Physics in Medicine and Biology, 59(23)

ISSN
0031-9155

Authors
Cho, H-M
Ding, H
Ziemer, BP
et al.

Publication Date
2014-12-07

DOI
10.1088/0031-9155/59/23/7211

Published in final edited form as:
Phys Med Biol. 2014 December 7; 59(23): 7211–7227. doi:10.1088/0031-9155/59/23/7211.

Energy response calibration of photon-counting detectors using X-ray fluorescence: a feasibility study

H-M Cho, **H Ding**, **BP Ziemer**, and **S Molloi**
Department of Radiological Sciences, University of California, Irvine, CA 92697

Abstract

Accurate energy calibration is critical for the application of energy-resolved photon-counting detectors in spectral imaging. The aim of this study is to investigate the feasibility of energy response calibration and characterization of a photon-counting detector using X-ray fluorescence. A comprehensive Monte Carlo simulation study was performed using Geant4 Application for Tomographic Emission (GATE) to investigate the optimal technique for X-ray fluorescence calibration. Simulations were conducted using a 100 kVp tungsten-anode spectra with 2.7 mm Al filter for a single pixel cadmium telluride (CdTe) detector with 3 × 3 mm^2 in detection area. The angular dependence of X-ray fluorescence and scatter background was investigated by varying the detection angle from 20° to 170° with respect to the beam direction. The effects of the detector material, shape, and size on the recorded X-ray fluorescence were investigated. The fluorescent material size effect was considered with and without the container for the fluorescent material. In order to provide validation for the simulation result, the angular dependence of X-ray fluorescence from five fluorescent materials was experimentally measured using a spectrometer. Finally, eleven of the fluorescent materials were used for energy calibration of a CZT-based photon-counting detector. The optimal detection angle was determined to be approximately at 120° with respect to the beam direction, which showed the highest fluorescence to scatter ratio (FSR) with a weak dependence on the fluorescent material size. The feasibility of X-ray fluorescence for energy calibration of photon-counting detectors in the diagnostic X-ray energy range was verified by successfully calibrating the energy response of a CZT-based photon-counting detector. The results of this study can be used as a guideline to implement the X-ray fluorescence calibration method for photon-counting detectors in a typical imaging laboratory.

Keywords

photon-counting detector; X-ray fluorescence; energy calibration

1. Introduction

Energy-resolved photon-counting X-ray detectors based on pulse height analysis have been investigated for medical X-ray imaging from the mid Nineties and have shown substantial advances with great potential to solve the current limitations of the traditional charge-

Corresponding Author and Reprint Address: Sabee Molloi, PhD, Department of Radiological Sciences, Medical Sciences I, B-140, University of California, Irvine, CA 92697, Fax: (949) 824-8115, Telephone: (949) 824-5904, symolloi@uci.edu.

integrating detectors (Taguchi and Iwanczyk, 2013). The commonly known advantages of the photon-counting detectors are: (1) the improvement of the contrast to noise ratio (CNR) by eliminating the electronic noise and by using optimal energy weighting, (2) the reduction of the radiation dose that is needed to acquire acceptable image quality by minimizing noise and improving CNR, and (3) the improvement of efficiency in material decomposition by minimizing the energy overlap in the spectral measurement (Le *et al.*, 2010; Le and Molloi, 2010). Since all of the above advantages are based on the energy discrimination capability of the photon-counting detector, it is important to have an accurate calibration between recorded pulse heights and the incident photon energies in order to realize all of the above advantages provided by photon-counting detectors (Fiederle *et al.*, 2008; Guni *et al.*, 2011; Ronaldson *et al.*, 2011).

In photon-counting detectors, the individual pixelated anodes on sensors such as cadmium telluride (CdTe) (Roessl and Proksa, 2007; Taguchi *et al.*, 2011), cadmium zinc telluride (CZT) (Shikhaliev, 2008; Le *et al.*, 2010), and silicon (Si) (Fredenberg *et al.*, 2010; Xu *et al.*, 2012) are connected to application-specific integrated circuits (ASICs). The ASICs contain charge sensitive preamplifiers, shaping amplifiers, multiple energy level threshold discriminators per preamplifier, and counters for each threshold discriminator (Taguchi and Iwanczyk, 2013). When photons strike the detector, the generated electrical charges produce a pulse, and the height of the pulse is compared to a user selectable threshold. A corresponding counter is incremented if the pulse height exceeds the threshold value. Small variations in the electrical performance of the threshold discriminator affect the performance of the spectral imaging detector by degrading the energy resolution. The calibration procedure needs to be performed for each discriminator by using individual calibration coefficients to set the thresholds of all detector pixels to one common energy value (Schlomka *et al.*, 2008).

Various energy calibration techniques using a mono-or poly-energetic spectrum have been previously used. The peak of the mono-energetic spectrum from synchrotron sources or radioactive isotopes was recorded against the known photon energy (Schlomka *et al.*, 2008; Koenig *et al.*, 2012; Barber *et al.*, 2009). Synchrotron radiation has added a new dimension to the use of x-rays in medical imaging and therapy, but also has extended beyond medical imaging (Suortti and Thomlinson, 2003; Meuli *et al.*, 2004). In that context, monochromatic synchrotron radiation is the ideal calibration source because of the ability to freely adjust both the calibration photon energy and flux. However, due to the prohibitive problems of space and cost, it is practically impossible to use a synchrotron as a routine detector energy calibration method in a standard imaging laboratory. Radioactive isotopes are more readily available in conventional imaging laboratories for detector calibration purposes. However, common isotopes which can be purchased without special permission generally have low activities. In order to achieve reasonable counting statistics, the calibration process can be very time-consuming, especially for large-area detectors. Using isotopes with high activity, on the other hand, raises the issues of safety and storage. The characteristic peak of a tungsten target (Wang *et al.*, 2009), the maximum energies of a poly-energetic spectrum (Taguchi *et al.*, 2011; Barber *et al.*, 2009), and the peak of a poly-energetic spectrum (Youn *et al.*, 2014) have been suggested as potential energy calibration method using standard x-

ray tubes. The method using tungsten characteristic peak information has several limitations. First of all, assuming a linear detector energy response, a minimum of two calibration photon energies will be required. The characteristic peak from a tungsten anode tube by itself will not be sufficient. Second, the peak can be severely contaminated by various detector spectral distortions, such as charge-sharing and pulse pileup, when measuring the direct beam (Wang *et al.*, 2011). Third, the characteristic peak of a tungsten target is only visible for tube voltages above 90 kVp for detectors with high quantum efficiency, such as a CdTe detector (Wang *et al.*, 2009). Therefore, applicable detector crystal material for this technique will be limited by detectors' quantum efficiency. Finally, the measurement of fluorescence peak width is a good estimation of the detector energy resolution, since the scattered signal is much lower than the fluorescence signal. It is not possible to use the characteristic peak from a poly-energetic spectrum, due to the strong signal from the primary beam. The accuracy of the maximum energy of a poly-energetic spectrum is also susceptible to the spectral distortions caused by pulse pileup effect. In this case quasicoincident photons will be recorded as a single count with a higher energy than their original energies due to the limited pulse resolving time in photon-counting detector (Taguchi *et al.*, 2011). Furthermore, any error in the tube calibration will propagate into the detector calibration. The accuracy and repeatability of the calibration method using the peak of the poly-energetic spectrum is limited since the peak of the poly-energetic spectrum is very broad. Therefore, despite the convenience, the calibration accuracy using a poly-energetic spectrum can also be problematic. Hence, development of a novel energy calibration technique, which is readily implementable in a standard imaging laboratory, as well as having high potential in terms of application, is needed.

X-ray fluorescence, which can be generated from the interaction between an X-ray beam and a high atomic number target, is a good source of calibration spectra with well-defined photon energies. The energy of the X-ray fluorescence is a characteristic of the target material since the electron binding energies depends on the atomic number (Bushberg and Boone, 2011). The mono-energetic X-ray spectra at various energies can be easily generated by using various fluorescent materials that can be used for detector energy calibration (Jakubek, 2011; Ballabriga *et al.*, 2011; Ronaldson *et al.*, 2011; van der Boog, 2013; Ballabriga *et al.*, 2013). However, the feasibility of X-ray fluorescence calibration has not been systematically studied in diagnostic energy range. In this work, we propose to calibrate the energy response of photon-counting detectors with an optimized X-ray fluorescence technique. A comprehensive Monte Carlo simulation study was carried out by considering various geometrical configurations such as angle, distance, detector type, and available fluorescent materials. The simulation results were validated using CdTe-based spectrometer. This technique was then applied to the CZT-based photon-counting detector to calibrate its energy response.

2. Methods

2.1. Monte Carlo Simulation

The GATE (Geant4 Application for Tomographic Emission) Monte Carlo simulation package V6 was used for all the simulations. The low energy package for processes between

250 eV and 100 GeV was chosen to simulate electromagnetic processes including de-excitation of the atom among three packages of models/cross-sections provided by GEANT4 (Jan *et al.*, 2011). Relevant low energy physics, including photoelectric, Compton scattering, and Rayleigh scattering, were modeled based on the evaluated data libraries. An extra library relating to atomic de-excitation was activated to simulate atomic shell effects, such as fluorescence emission and Auger electron production (Chauvie *et al.*, 2001). However, only the fluorescent material was specified as the de-excitation region. The background counts from Compton and elastically scattered x-ray photons can be obtained by deactivating atomic de-excitation.

2.2. X-ray beam condition

A polychromatic X-ray energy spectrum with tungsten target was simulated using SpekCalc program (Poludniowski *et al.*, 2009). The simulated photons are emitted from a small square focal spot, 0.3×0.3 mm^2, within a certain cone angle to cover the volume of fluorescent material. The exposed cone angle could be adjusted according to the study purpose, which is equivalent to the experimental approach of modifying the beam collimator. A 100 kVp spectrum with 2.7 mm aluminum (Al) filter was used in all simulations except for a uranium compound, which needed a 150 kVp with 2.7 mm Al filter. The total number of photons was properly selected in each study to balance the simulation time and the statistical noise.

2.3. System geometry

The simulated system geometry is shown in figure 1. The fluorescent material was modeled with a homogeneous cylindrical volume. The generated X-ray fluorescence from the fluorescent material was detected by a simulated CdTe-based photon-counting detector. When not investigating the geometrical distance dependence, two different settings were used for the source to fluorescent material distance (SOD) and the fluorescent material to detector distance (ODD) depending on the parameters studied. Geometry with a short SOD and ODD was used when the investigated parameters not affected by the distance, for instance, the detection angle, fluorescent material size, and detector crystal material. In contrast, practical SOD and ODD geometry were used when the investigated parameters were relevant to the distance, for example, the detector shape and size effect.

2.3.1. Angular dependence—The detection angle, defined as the angle between the forward direction of the primary beam and the detector, varied from 20° to 170° in 10° incremental steps to investigate angular dependence of X-ray fluorescence and scatter background. Both the SOD and ODD were initially set as 3 cm in the angular dependence study. The number of primary photons was 1×10^9 for each measurement. A total of six fluorescent materials (Ag_2O, $C_{19}H_{26}I_3N_3O_9$, $BaSO_4$, $C_{16}H_{28}GdN_5O_9$, HfO_2, and $HAuCl_4$) with diameter of 6 mm were simulated. Figure 2 shows the linear attenuation coefficient of the six simulated fluorescent materials. When measuring the angular dependence of the scatter background, the integrated counts within three standard deviations from the K_α peak energy for each fluorescent material were recorded. The X-ray fluorescence-to-scatter ratio (FSR), which was calculated by the ratio of fluorescence peak and the scatter background, was used as the figure of merit for performance.

2.3.2. Geometrical distance dependence—The recorded X-ray fluorescence intensity will increase monotonically as one reduces the SOD and ODD. However, in the experimental environment, the minimum SOD and ODD available can be limited by the size of X-ray tube and detector. Various SOD and ODD conditions were simulated in order to investigate the relation between X-ray fluorescence intensity and distance. First, the SOD was increased from 10 to 100 cm with a fixed ODD of 20 cm. Then, the ODD was varied from 5 to 100 cm with a fixed SOD of 50 cm. A fluorescent material made of $BaSO_4$ with diameter of 6 mm was used. The detection angle was fixed at 120°, and the number of primary photons was 1×10^9 in each measurement.

2.4. Detector

A $3 \times 3 \times 1$ mm^3 CdTe-based photon-counting detector, with the same specifications as the CdTe-based spectrometer, was used for all simulations except the investigations of the detector crystal material. A CdTe-based spectrometer was used for validation of the simulation results. A detector collimator is typically used in X-ray fluorescence studies to minimize background scatter by reducing the incident angle to the detector. A detector collimator was not simulated since the source of scatter was minimized by only activating the atomic de-excitation function for the fluorescent material. A total of 5×10^8 primary photons were simulated, and the detection angle was 120° when the effect of detector crystal material, size, and shape was evaluated.

2.4.1. Detector crystal materials—For the investigation of the detector crystal material, CZT, CdTe, and Si were simulated as a crystal material in the same size and geometry. The SOD and ODD were both set as 3 cm. The intensities of the recorded X-ray fluorescence from the six fluorescent materials (Ag_2O, $BaSO_4$, $C_{16}H_{28}GdN_5O_9$, HfO_2, $HAuCl_4$, and $UO_2(NO_3)_2$) with diameter of 6 mm were compared.

2.4.2. Geometrical structure of detector—For the investigations of the detector structure, area detectors with side lengths of 3, 6, 12, 24, and 48 mm and the line detector with lengths of 12, 30, 60, 120, and 240 mm were simulated. The pixel size was kept as 3 mm for all different sizes of the detector. A fluorescent material made of $BaSO_4$ with diameter of 6 mm was used, and the SOD and ODD were set as 30 cm. The effects of various detector shapes and sizes were evaluated using the intensity and energy resolution of K_α peak of Ba.

2.5. Fluorescent materials

The thirteen fluorescent materials readily available in the typical laboratory, energy range from 10 to 100 keV, are described in table 1. Different combinations of these fluorescent materials were used in both simulation and experiment depending on each study's purpose.

The fluorescent material shape and size effect was investigated in the simulation. A cylinder, box, and sphere shape phantom was investigated under the same data acquisition condition. A cylindrical shape fluorescent material was used for all the other studies in this article.

The fluorescent material size effect was considered in two approaches. In the first approach, $BaSO_4$ with diameter of 6, 30, 60 and 120 mm without a container were studied at five different detection angles, 30°, 60°, 90°, 120°, and 150°. Both SOD and ODD were set as 10 cm. The incident X-ray beam angle was changed according to the fluorescent material size in order to cover the whole target under the number of primary photons, 5×10^8. In the second approach, 1 to 5 mm thicknesses of container wall that was made of polymethyl methacrylate (PMMA) for fluorescent material was studied using a detection angle of 120°. The fluorescent material with a diameter of 6 mm without container was used as reference data. Six fluorescent materials (KBr, Ag_2O, $BaSO_4$, $C_{16}H_{28}GdN_5O_9$, HfO_2, and $HAuCl_4$), whose K_α fluorescence energies are approximately 10 keV apart, were simulated in order to investigate the intensity reduction of each material's X-ray fluorescence by container wall thickness. This result can be a guide-line when choosing the container for fluorescent material.

2.6. Experimental studies

2.6.1. CdTe-based spectrometer for simulation validation study—To validate the simulation results, experiments were designed to investigate the angular dependence of the X-ray fluorescence using a CdTe-based spectrometer (X-123, Amptek Inc., MA). The small size of the spectrometer allowed a precise angular setup without concern about primary x-ray detection. As shown in figure 3(a), the SOD and ODD were set at approximately 95 cm and 14 cm, respectively. The X-ray beam (100 kVp, 4mA with 2.7 mm Al) was generated by a tungsten target 160 watt X-ray tube (XRB101, Spellman, Hauppauge, NY). The X-ray beam was collimated by a 2.7 mm diameter lead pinhole collimator to produce a small cone angle that fit the object size. Five different fluorescent materials (Ag_2O, iodinated contrast agent, $BaSO_4$, gadodiamide contrast agent, and $HAuCl_4$) were placed in plastic cylindrical containers with inner diameter of 6 mm and wall thickness of 0.7 mm. The detection angle was changed from 30° to 150° with an incremental step of 30°. A specially designed cylindrical-shaped copper pinhole collimator with a lead sleeve of 1.9 mm thick and an opening of 1.6 mm was used to minimize the unwanted background scatter counts (figure 3(b)). A scan time of 60 sec was used.

2.6.2. CZT-based photon-counting detector for application study—In a direct application, the proposed X-ray fluorescence calibration technique was performed with a CZT-based photon-counting detector (eV2500, eV Microelectronics Inc., Saxonburg, PA) (Le *et al.*, 2010; Le and Molloi, 2010) which is more sensitive to the energy calibration of each pixel due to its design for imaging with multiple pixels as compared with the spectrometer. The detector consisted of a single row of four CZT crystals of 12.8 mm in length and 3 mm in thickness. Each crystal consisted of 16 pixels with a pixel pitch of 0.8 mm. The spectra from one of the pixels were used. The same X-ray tube and beam condition as the above validation study using CdTe spectrometer were used. The X-ray beam was collimated by a brass 14.5 mm diameter cylindrical pinhole collimator. The detector was positioned at 120° with respect to the incident X-ray beam direction according to the optimized simulation results. The CZT detector used 10-bit digital-to-analog converter (DAC) pulse height comparator from 0 to 2.5 V. Each DAC step corresponds to approximately 2.44 mV. Each spectrum was acquired within a frame time of 0.5 sec and a

step of 1 DAC. A total of 300 DAC steps, 150 DAC below and above the fluorescence peak, were acquired and took approximately 2.5 minutes for each spectrum. Since the linear range of the detector is less than 1.2×10^6 count per second per square millimeter (cps/mm^2), a flux of 0.8×10^6 cps/mm^2 was used to minimize pulse pileup (Ding and Molloi, 2012). The K_α peak centers of five fluorescent materials ($NbCl_5$, iodinated contrast agent, gadodiamide contrast agent, HfO_2, and $Pb(NO_3)_2$) were recorded during the energy calibration procedure. To calibrate the measured pulse height of the incident photon energy, peak centers in unit of DAC were plotted as a function of the known X-ray fluorescence energies in unit of keV, and linear regression analysis was performed. Furthermore, the K_α peak centers of another six fluorescent materials (Ag_2O, $BaSO_4$, CeO_2, Ho_2O_3, W, and $HAuCl_4$) were recorded in unit of energy after applying energy calibration. The accuracy of the energy calibration was evaluated by calculating root-mean-square (RMS) errors between known and recorded X-ray fluorescence peak energy.

3. Results

3.1. System geometry

3.1.1. Angular dependence—The X-ray fluorescence and scatter background detection angle dependence were investigatedfor six fluorescent materials; Ag_2O, $C_{19}H_{26}I_3N_3O_9$, $BaSO_4$, $C_{16}H_{28}GdN_5O_9$, HfO_2, and $HAuCl_4$. Figure 4(a) shows the angular dependence of the detected K_α peak of each fluorescent material. The X-ray fluorescence intensity increased with increasing detection angle. The angular dependence of scatter background, integrated counts within three standard deviations from the K_α peak energy for each fluorescent material is shown in figure 4(b). Figure 4(a) and (b) were normalized to the counts of Ag's K_α peak at 170° to compare with experimental result. The minimum scatter background was shown in the range of 80° to 120° but detection angle which showed maximum background scatter was located at 20° for the $C_{19}H_{26}I_3N_3O_9$, $C_{16}H_{28}GdN_5O_9$, and $HAuCl_4$ compounds and at 170° for Ag_2O, $BaSO_4$, and HfO_2. The X-ray FSR for all tested fluorescent materials was maximized at a back detection angle range of 100° to 140° (figure 4(c)).

3.1.2. Geometrical distance dependence—Figure 5 shows the X-ray fluorescence intensity reduction according to the fluorescent material to source and detector distances. The degree of the reduction in the recorded fluorescence intensity was different for the SOD and ODD.

3.2. Detector

3.2.1. Detector crystal materials—The detected k-shell fluorescence intensity of six fluorescent materials with the three different detector materials is shown in figure 6. A usable fluorescent material is limited by each detector material's quantum detection efficiency, which is affected by the X-ray stopping power for the X-ray fluorescence energy. The CdTe and CZT show high detection efficiency for the fluorescent X-ray photons from all the fluorescent materials in the energy range of 20 to 100 keV, while Si shows low detection efficiency for higher energies.

3.2.2. Geometrical structure of detector—Figure 7(a) shows the pixel variation of X-ray fluorescence intensity according to the size of line detector from 12 to 240 mm. The pixel variation mainly followed the angular dependence results of the X-ray fluorescence (figure 4). The angular range of 98° to 142° corresponds to the range from the first to the last pixels of a 240 mm line detector, respectively. The standard deviation of the measured energy resolution from the combined spectrum from all the pixels was 4 % and 7 % for area and line detectors according to the size, respectively (figure 7(b)). It shows that different detection angles in each pixel, due to shape or size of the detector, is not a critical factor that broadens the recorded fluorescence peaks.

3.3. Fluorescent materials

The X-ray FSR difference between the three different object shapes was small enough to be negligible. The X-ray FSR according to the object size is shown in figure 8 at five different detection angles. For sizes less than 60 mm in diameter, the highest FSR was found at 120°. The attenuation of both incident X-ray and generated X-ray fluorescence by the fluorescent materials themselves were more dominant at smaller detection angles than the larger angles. This phenomenon still remained for objects with diameter of 120 mm at 120°. Larger objects generate a higher number of X-ray fluorescence at 150°. The lower X-ray fluorescence energy materials showed higher degree of attenuation as a function of the container wall thickness. The attenuation is approximately 20 % with 5 mm wall thickness for fluorescent materials that have higher than 50 keV X-ray fluorescence energy.

3.4. Experimental study

3.4.1. CdTe-based spectrometer for simulation validation study—The simulation results were validated by the experimentally measured angular dependence of five fluorescent materials using CdTe-based spectrometer (figure 4(d)). The experimental results were normalized with respect to the counts from Ag's K_α peak at 150° to compare with simulation results. The angular dependence of all fluorescent materials from the experiment showed the same trend with simulation even though a larger detection angle increment was used in the experimental study.

3.4.2. CZT-based photon-counting detector for application study—The central DAC values for five fluorescent materials' K_α peak acquired from CZT-based photon-counting detector were recorded and plotted as a function of the known fluorescence energy in figure 9 (a). Linear regression analysis was performed to calibrate the recorded DAC value to the incident X-ray fluorescence energy. The gain and offset were determined as 3.4 DAC/keV and 59.25 DAC, respectively. Additionally, six fluorescent materials were used to verify the energy calibration (figure 9 (b)). The recorded energies of each material's fluorescence peak showed that the energy calibration was properly performed. The RMS errors between known and recorded fluorescence peak energy were calculated to be 0.14 keV. The maximum difference of the recorded K_α and K_β peak energies from known fluorescence energies were 0.5 keV and 0.7 keV, respectively.

4. Discussion

An accurate energy calibration is a critical procedural step for the implementation of energy-resolved photon-counting detectors in spectral imaging. The X-ray fluorescence calibration technique has been proposed to replace typical energy calibration method using synchrotron and isotope sources. A major issue to resolve before using X-ray fluorescence technique is how to minimize unwanted background from Compton and elastically scattered X-ray photons and fluorescence X-ray photons from other elements in the beam path (Bazalova *et al.*, 2012; Cheong *et al.*, 2010; Ren *et al.*, 2014). Therefore, geometric optimization is essential for X-ray fluorescence acquisition to maximize signal to noise ratio (Ahmad *et al.*, 2014). The dependence of X-ray fluorescence spectra on the detector crystal materials and geometrical structures was investigated in this study. Numerous usable fluorescent materials which can be easily obtained in the typical laboratory were evaluated in simulation and validated in experimental studies. The size of the fluorescent material and the thickness of the container wall were also investigated. The study demonstrates the importance of optimizing not only the fluorescent material for calibration according to the purposed photon-counting detector's crystal material, but also the geometric configuration.

4.1. System geometry

The X-ray fluorescence produced by an atom is isotropic and has uniform intensity over all angles with fixed energies. However, our simulation and experimental results suggested an angular dependence of the optimal detection of X-ray fluorescence (figure 4(a)). This is due to the attenuation of the primary beam as it passes through an object. Thus, the number of photons that can generate X-ray fluorescence in the forward angles is reduced as compared with the backward angles. The degree of angular dependence for different fluorescent materials varies depending on their linear attenuation coefficients (figure 2). Since we used a poly-energetic incident X-ray spectrum, the number of photons above the K-edge energy of each fluorescent material decreased as the material's K-edge energy increased. The three fluorescent materials, $C_{19}H_{26}I_3N_3O_9$, $C_{16}H_{28}GdN_5O_9$, and $HAuCl_4$, generate a higher number of scatter due to the higher number of hydrogen atoms, which increases the probability of Compton interaction. Also, these three fluorescent materials have lower linear attenuation coefficient by themselves (figure 2). Therefore, the scattered photons of these three fluorescent materials show higher intensity toward the forward direction at low angles than other fluorescent materials (figure 4(b)).

The distance between the fluorescent material to the X-ray source and the detector will affect the detected X-ray fluorescence intensity. Therefore, it will determine the data acquisition time needed to record sufficient photon statistics. In the experiment, the minimum distance to the fluorescent material was limited by the geometrical size of the X-ray source and the detector. The simulation result about the SOD and ODD provided criteria for selecting the optimal imaging geometry. Basically, the intensity of the detected X-ray fluorescence is related to three factors: the exposed volume of the fluorescent material, the Beer Lambert law, and the inverse square law. In this study, the attenuations of the primary X-ray and generated X-ray fluorescence by the fluorescent material itself were constant since the detection angle was fixed at 120°. Therefore, the change of the X-ray fluorescence

intensity according to the SOD (figure 5) can be explained by the combination of two factors: the intersection volume change and inverse square law. The area covered by the incident X-ray beam at the fluorescent material position increased as the SOD increased, and the area also affected the detected X-ray fluorescence intensity. On the contrary, the ODD is only related to the inverse square law (figure 5). These differences between SOD and ODD would happen only if the volume of the detectable fluorescent material is larger than the volume of the fluorescent material covered by the incident X-ray beam.

4.2. Detector

The X-ray stopping power of the detector depends on the detector material and thickness. Three different detector materials which are typically employed as a semiconductor crystal material in current photon-counting technology, CdTe, CZT, and Si, were simulated with identical thickness to detect the X-ray fluorescence in the range from 20 to 100 kVp. The difference between CZT and CdTe in terms of mass fraction of contents is only 5%, due to the presence of zinc in the CZT (Eisen *et al.*, 1999). The 5% difference didn't affect the detected intensity results. In contrast, Si showed significantly lower intensity than those of the other two materials within the energy range, due to a relatively small atomic number. Even at a 120° detection angle where the FSR was shown to be the greatest, the extremely low intensity of X-ray fluorescence from Au and U made these signals difficult to distinguish from the background scatter. Based on this result, proper fluorescent materials can be chosen by considering detectable X-ray fluorescence energy range depending on the particular detector material.

The variation of X-ray fluorescence intensity and energy resolution for different pixels of different detector sizes and shapes were investigated assuming an ideal detector by ignoring the effect of electronics on energy resolution. The currently available sizes of the photon-counting detectors were considered (Taguchi and Iwanczyk, 2013). The results indicate that the detection angle difference in each pixel affected the intensity of the detected X-ray fluorescence peak, but it did not affect its width. The signal response variation due to the detector crystal's nonuniformity or the charge spread due to the detector thickness will be a more dominant factor to degrade energy resolution of the detector than the detection angle (Shikhaliev, 2008; He *et al.*, 1998).

4.3. Fluorescent materials

The choice of the material, which will generate X-ray fluorescence, is the most important task in this study. To implement the proposed technique in a typical imaging laboratory, the fluorescent material should be easy to find and should cover the energy range of diagnostic medical imaging. Not only the primary signals from k-shell fluorescence (k_α and k_β), but also from other shells (L or M) of each fluorescent material will clearly identify with an ideal detector. However, the k_α and k_β peak differentiability and the other shells' signal strength will be degraded by the limited energy resolution, low sensitivity, and high scatter background of the actual detector. However, even considering the degradation of the signal intensity in the experiment, more than thirteen data points from the k_α and k_β peak of each fluorescent material can be used, which will be sufficient to calibrate the energy response of a detector or to estimate the detector response function in the energy range of 10 ~ 110 keV.

Since all the proposed fluorescent materials are in powder or liquid format, a container is needed. The intensity of the generated X-ray fluorescence will increase by using a larger volume of the fluorescent material, but the attenuation of the incident X-ray and X-ray fluorescence will also increase by the fluorescent material itself. In addition, the thickness of the container wall will introduce additional attenuation, especially for low energy X-ray fluorescence. The simulation results show that the detection angle of 120° offers a broad choice of container sizes within the 60 mm limit for an inner diameter. Since the trends of FSR distribution according to the detection angles in all other fluorescent materials are similar to those with $BaSO_4$, this result can be applied to other fluorescent materials. As expected, the container wall thickness mostly affected the low energy X-ray fluorescence; therefore less than 1 mm container wall thickness is recommended for calibration data points around 10 keV. Since the size of the fluorescent material is small (< 6 mm) and the scatter portion is relatively smaller than the fluorescence signal, different shapes of the phantom didn't produce large differences in FSR.

4.4. Experimental study

Experimental results of angular dependence for X-ray fluorescence were in good agreement with the simulation results. Simulation data for angular dependence of the X-ray fluorescence was acquired in smaller step increment with more precise geometric alignment between incident X-ray beam and the detector than those of the experimental study.

An excellent linear energy response was found for the CZT detector within the investigated energy range (figure 9 (a)). K_α peak of all fluorescent materials were well detected (figure 9 (b)). However, K_β peaks were detected only from the fluorescent materials that have a larger energy difference between K_α and K_β than the detector energy resolution of 6 keV. Due to the lower proportion of the K_β than K_α, the recorded energy of K_β peak showed less accuracy than those of K_α. Two fluorescent materials (KBr and $UO_2(NO_3)_2$) listed in table 1 were not included in CZT detector study. KBr was excluded, since the electronic noise floor of studied CZT detector was at 22 keV, which is above the fluorescence peak from Br (Le and Molloi, 2010). Measurement from $UO_2(NO_3)_2$ was limited by the small amount of the material available. In practical usage, two or three data points, which are separated enough to cover large energy range from the fluorescence materials are easy to get in each laboratory and will be sufficient to measure energy calibration curve if the investigated detector has good linearity. Further studies about the detector response function estimation using the X-ray fluorescence technique are currently under investigation.

4.5. Study limitations

The simulation study was designed to investigate the effect of geometrical parameters on X-ray fluorescence detection. Therefore, the simulation of the detector configuration was simplified by excluding the effect of detection electronics. The pulse pileup effect, which is a well-known spectrum distortion factor in photon-counting detectors, was not simulated because the modeled CdTe photon-counting detector usually use well-designed pinhole collimator (Ren *et al.*, 2014) to reduce the total number of photons specifically to avoid pulse pileup distortion. In addition, the degradation of the spectrum by charge-sharing in adjacent pixels was ignored due to the fact that a single pixel spectrometer was used.

However, since all physical interactions are modeled in the simulation, quasi-coincident events in the same pixel (Taguchi and Iwanczyk, 2013) were implemented. Therefore, the angular dependence of X-ray fluorescence was shown to be in good agreement with the experimental results, although the amount of overall background scatter was less than experimental results by activating the atomic de-excitation function only on the fluorescent material.

In the study using a CZT-based photon-counting detector, only one pixel was calibrated. The same calibration procedure can be repeated for all the pixels to minimize the pixel variation in the image. Depending on the particular detector, the gain and offset from each pixel can be applied directly into the comparator (Barber *et al.*, 2009; Taguchi *et al.*, 2011) in the form of a mean gain and offset with standard deviation or it can be applied after data acquisition in the form of a calibration map (Youn *et al.*, 2014). Accurate energy calibration of each pixel should improve the performance of the detector in spectral imaging.

The feasibility of thirteen fluorescent materials was investigated by simulation and validated by an experimental study. The selection of these fluorescent materials was based on their fluorescence energies spaced by approximately 10 keV, as well as on the ease of obtaining the materials in a typical laboratory. The possible calibration energy range covered by the proposed fluorescent materials ranged from 10 to 110 keV, which is the upper limit of a stable material. However, the energy range of diagnostic medical X-ray imaging can extend up to 150 keV (Bushberg and Boone, 2011). Since CZT-based photon-counting detector has a linear response, the energy calibration result from low energy range could be applied to higher energies. To investigate the potential error when applying lower energy range calibration to higher energy data, we applied energy calibration acquired from energy range of 10 to 35 keV to the spectra in the energy range of 40 to 80 keV. The RMS error of all recorded energies and the maximum difference between the known and recorded K_α peak energy were 0.48 keV and 1.69 keV, respectively. Since the potential error is much smaller than the energy resolution of the detector, the proposed method can be used in the whole energy range of diagnostic medical X-ray imaging.

5. Conclusions

An X-ray fluorescence based energy calibration technique for photon-counting detectors was proposed. The technical feasibility and the geometrical effect of the system configuration were investigated by simulation and validated by experiment. The optimal detection angle was determined to be approximately at 120° with respect to the beam direction, which showed the highest FSR with weak fluorescent material size dependence. The effects of the detector material, shape, and size on the recorded X-ray fluorescence were investigated. The intensity of X-ray fluorescence could be controlled by adjusting the distance between the X-ray source, the object, and the detector. The signal intensity could also be affected by the container wall thickness. With an optimized configuration, we demonstrated the feasibility of using X-ray fluorescence for energy calibration of photon-counting detector in the diagnostic X-ray energy range. The results of this study can be used as a guideline to implement the X-ray fluorescence calibration method for photon-counting detectors in a typical imaging laboratory.

Acknowledgments

This work was supported in part by NIH/NCI grant R01CA13687.

References

Ahmad M, Bazalova M, Xiang L, Xing L. Order of Magnitude Sensitivity Increase in X-Ray Fluorescence Computed Tomography (XFCT) Imaging With an Optimized Spectro-Spatial Detector Configuration: Theory and Simulation. 2014

Ballabriga R, Alozy J, Blaj G, Campbell M, Fiederle M, Frojdh E, Heijne E, Llopart X, Pichotka M, Procz S. The Medipix3RX: a high resolution, zero dead-time pixel detector readout chip allowing spectroscopic imaging. Journal of Instrumentation. 2013; 8:C02016.

Ballabriga R, Blaj G, Campbell M, Fiederle M, Greiffenberg D, Heijne E, Llopart X, Plackett R, Procz S, Tlustos L. Characterization of the Medipix3 pixel readout chip. Journal of Instrumentation. 2011; 6:C01052.

Barber, WC.; Nygard, E.; Iwanczyk, JS.; Zhang, M.; Frey, EC.; Tsui, BM.; Wessel, JC.; Malakhov, N.; Wawrzyniak, G.; Hartsough, NE. SPIE Medical Imaging. International Society for Optics and Photonics; 2009. Characterization of a novel photon counting detector for clinical CT: count rate, energy resolution, and noise performance; p. 725824-9.

Bazalova M, Kuang Y, Pratx G, Xing L. Investigation of x-ray fluorescence computed tomography (XFCT) and K-edge imaging. Medical Imaging, IEEE Transactions on. 2012; 31:1620–7.

Bushberg, JT.; Boone, JM. The essential physics of medical imaging. Lippincott Williams & Wilkins; 2011.

Chauvie S, Depaola G, Ivanchenko V, Longo F, Nieminen P, Pia M. Geant4 low energy electromagnetic physics. In. Proc Computing in High Energy and Nuclear Physics. 2001:337–40.

Cheong S-K, Jones BL, Siddiqi AK, Liu F, Manohar N, Cho SH. X-ray fluorescence computed tomography (XFCT) imaging of gold nanoparticle-loaded objects using 110 kVp x-rays. Physics in medicine and biology. 2010; 55:647. [PubMed: 20071757]

Ding H, Molloi S. Image-based spectral distortion correction for photon-counting x-ray detectors. Medical physics. 2012; 39:1864–76. [PubMed: 22482608]

Eisen Y, Shor A, Mardor I. CdTe and CdZnTe gamma ray detectors for medical and industrial imaging systems. Nuclear Instruments and Methods in Physics Research Section A: Accelerators, Spectrometers, Detectors and Associated Equipment. 1999; 428:158–70.

Fiederle M, Greiffenberg D, Idárraga J, Jakůbek J, Král V, Lebel C, Leroy C, Lord G, Pospíšil S, Sochor V. Energy calibration measurements of MediPix2. Nuclear Instruments and Methods in Physics Research Section A: Accelerators, Spectrometers, Detectors and Associated Equipment. 2008; 591:75–9.

Fredenberg E, Lundqvist M, Cederström B, Åslund M, Danielsson M. Energy resolution of a photon-counting silicon strip detector. Nuclear Instruments and Methods in Physics Research Section A: Accelerators, Spectrometers, Detectors and Associated Equipment. 2010; 613:156–62.

Guni E, Durst J, Kreisler B, Michel T, Anton G, Fiederle M, Fauler A, Zwerger A. The influence of pixel pitch and electrode pad size on the spectroscopic performance of a photon counting pixel detector with CdTe sensor. Nuclear Science, IEEE Transactions on. 2011; 58:17–25.

He Z, Knoll G, Wehe D, Du Y. Coplanar grid patterns and their effect on energy resolution of CdZnTe detectors. Nuclear Instruments and Methods in Physics Research Section A: Accelerators, Spectrometers, Detectors and Associated Equipment. 1998; 411:107–13.

Jakubek J. Precise energy calibration of pixel detector working in time-over-threshold mode. Nuclear Instruments and Methods in Physics Research Section A: Accelerators, Spectrometers, Detectors and Associated Equipment. 2011; 633:S262–S6.

Jan S, Benoit D, Becheva E, Carlier T, Cassol F, Descourt P, Frisson T, Grevillot L, Guigues L, Maigne L. GATE V6: a major enhancement of the GATE simulation platform enabling modelling of CT and radiotherapy. Physics in medicine and biology. 2011; 56:881. [PubMed: 21248393]

Koenig T, Schulze J, Zuber M, Rink K, Butzer J, Hamann E, Cecilia A, Zwerger A, Fauler A, Fiederle M. Imaging properties of small-pixel spectroscopic x-ray detectors based on cadmium telluride sensors. Physics in medicine and biology. 2012; 57:6743. [PubMed: 23032372]

Le HQ, Ducote JL, Molloi S. Radiation dose reduction using a CdZnTe-based computed tomography system: Comparison to flat-panel detectors. Medical physics. 2010; 37:1225–36. [PubMed: 20384260]

Le HQ, Molloi S. Segmentation and quantification of materials with energy discriminating computed tomography: A phantom study. Medical physics. 2010; 38:228–37. [PubMed: 21361191]

Meuli R, Hwu Y, Je JH, Margaritondo G. Synchrotron radiation in radiology: radiology techniques based on synchrotron sources. European radiology. 2004; 14:1550–60. [PubMed: 15316744]

Poludniowski G, Landry G, DeBlois F, Evans P, Verhaegen F. SpekCalc: a program to calculate photon spectra from tungsten anode x-ray tubes. Physics in medicine and biology. 2009; 54:N433. [PubMed: 19724100]

Ren L, Wu D, Li Y, Wang G, Wu X, Liu H. Three-dimensional x-ray fluorescence mapping of a gold nanoparticle-loaded phantom. Medical physics. 2014; 41:031902. [PubMed: 24593720]

Roessl E, Proksa R. K-edge imaging in x-ray computed tomography using multi-bin photon counting detectors. Phys Med Biol. 2007; 52:4679–96. [PubMed: 17634657]

Ronaldson J, Walsh M, Nik S, Donaldson J, Doesburg R, van Leeuwen D, Ballabriga R, Clyne M, Butler A, Butler P. Characterization of Medipix3 with the MARS readout and software. Journal of Instrumentation. 2011; 6:C01056.

Schlomka J, Roessl E, Dorscheid R, Dill S, Martens G, Istel T, Bäumer C, Herrmann C, Steadman R, Zeitler G. Experimental feasibility of multi-energy photon-counting K-edge imaging in preclinical computed tomography. Physics in medicine and biology. 2008; 53:4031. [PubMed: 18612175]

Shikhaliev PM. Computed tomography with energy-resolved detection: a feasibility study. Phys Med Biol. 2008; 53:1475–95. [PubMed: 18296774]

Suortti P, Thomlinson W. Medical applications of synchrotron radiation. Physics in medicine and biology. 2003; 48:R1–35. [PubMed: 12884920]

Taguchi K, Iwanczyk JS. Vision 20/20: Single photon counting x-ray detectors in medical imaging. Medical physics. 2013; 40:100901. [PubMed: 24089889]

Taguchi K, Zhang M, Frey EC, Wang X, Iwanczyk JS, Nygard E, Hartsough NE, Tsui BM, Barber WC. Modeling the performance of a photon counting x-ray detector for CT: Energy response and pulse pileup effects. Medical physics. 2011; 38:1089–102. [PubMed: 21452746]

van der Boog R. 2013Energy calibration procedure of a pixel detector.

Wang, X.; Meier, D.; Sundal, BM.; Oya, P.; Maehlum, GE.; Wagenaar, DJ.; Patt, BE.; Tsui, BM.; Frey, EC. A digital line-camera for energy resolved x-ray photon counting. Nuclear Science Symposium Conference Record (NSS/MIC), 2009 IEEE; IEEE; 2009. p. 3453-7.

Wang X, Meier D, Taguchi K, Wagenaar DJ, Patt BE, Frey EC. Material separation in x-ray CT with energy resolved photon-counting detectors. In. Proceedings of SP1E. 2011:79611V.

Xu C, Danielsson M, Karlsson S, Svensson C, Bornefalk H. Preliminary evaluation of a silicon strip detector for photon-counting spectral CT. Nuclear Instruments and Methods in Physics Research Section A: Accelerators, Spectrometers, Detectors and Associated Equipment. 2012; 677:45–51.

Youn H, Han JC, Kam S, Yun S, Kim HK. Energy calibration of energy-resolved photon-counting pixel detectors using laboratory polychromatic x-ray beams. Nuclear Instruments and Methods in Physics Research Section A: Accelerators, Spectrometers, Detectors and Associated Equipment. 2014

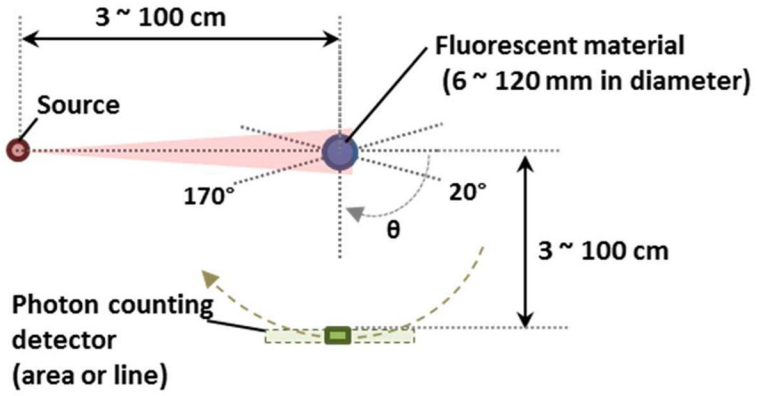

Figure 1.

Schematic diagram of the simulated system geometry for X-ray fluorescence. Each of the geometrical parameters was investigated by changing their setup in order to evaluate the effect of each parameter on X-ray fluorescence measurement.

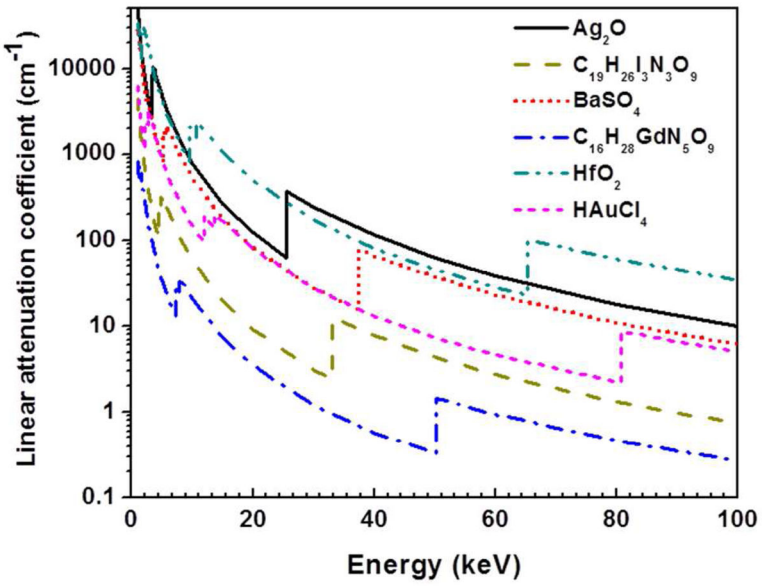

Figure 2.

The linear attenuation coefficient of the six fluorescent materials that were used in the angular dependence study.

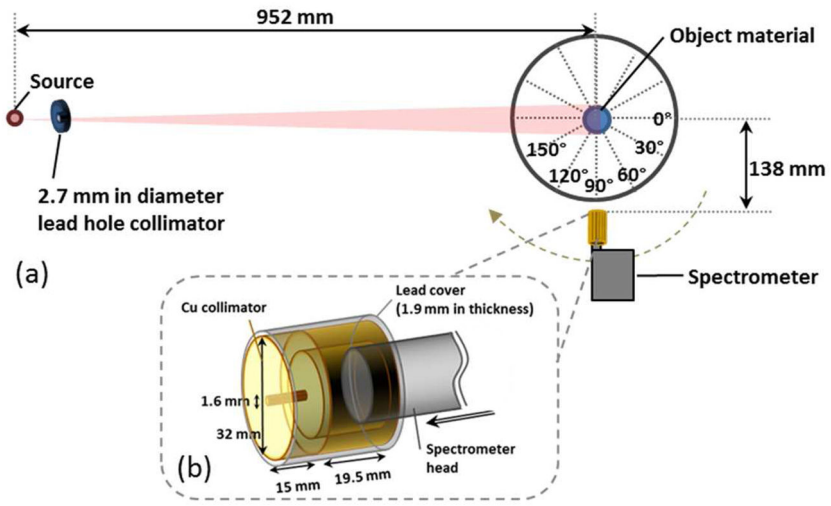

Figure 3.

Schematic diagrams of (a) the experimental setup for simulation validation study and (b) detector collimator.

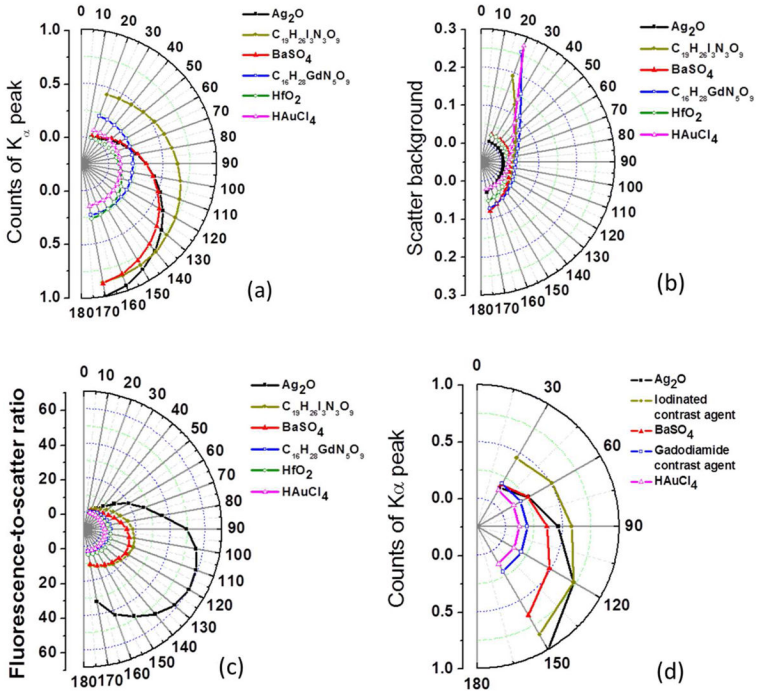

Figure 4.

The detection angle dependence of (a) the X-ray fluorescence, (b) the scatter background, and (c) the X-ray FSR of six fluorescent materials were simulated from 20° to 170° with an incremental step of 10°. (d) The detection angle dependence of the X-ray fluorescence of five materials were experimentally measured from 30° to 150° with an incremental step of 30°.

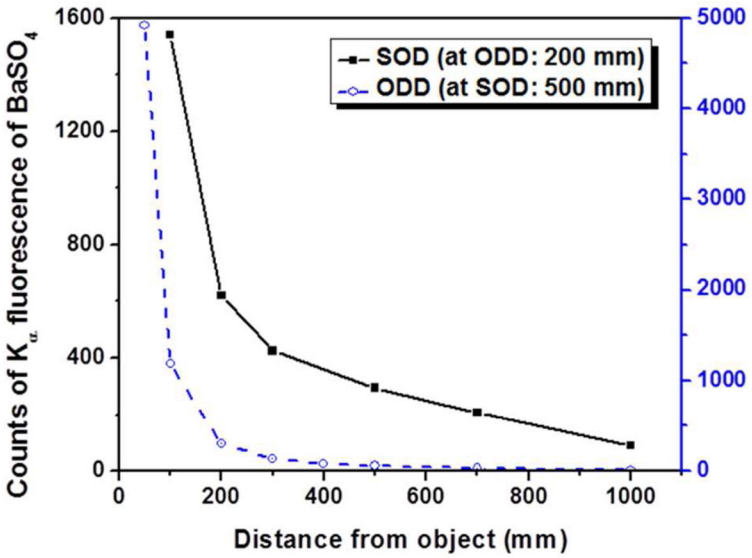

Figure 5.

The SOD and ODD dependence of X-ray fluorescence intensity from $BaSO_4$. The y-axis on the left and right side of the chart indicates SOD (solid square with line) and ODD (open square with dashed line), respectively.

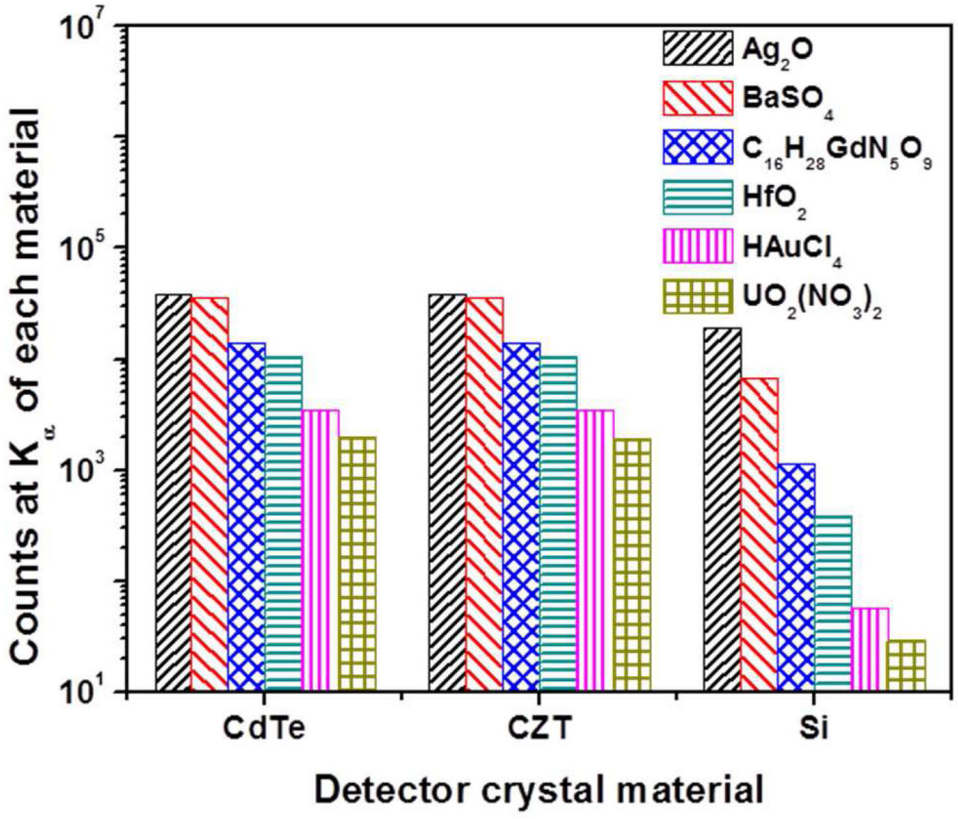

Figure 6.
Detected k-shell fluorescence intensity of six fluorescent materials according to the detector crystal material.

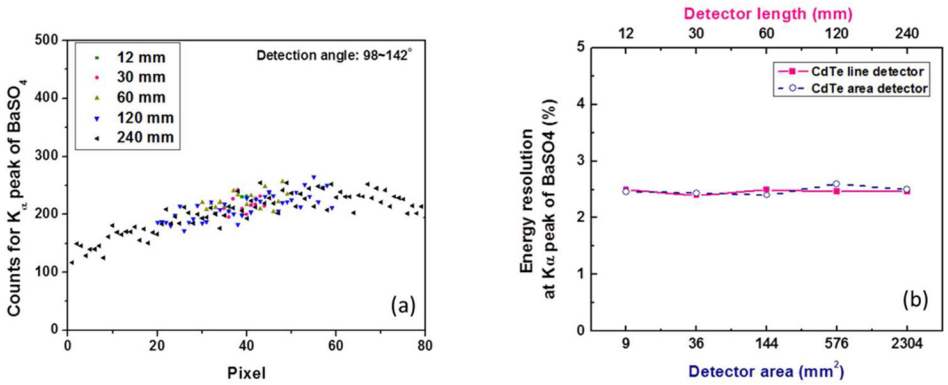

Figure 7.

(a) A pixel variation of detected intensity of X-ray fluorescence from $BaSO_4$ in the line detector. (b) The energy resolution measured for all the pixels using X-ray fluorescence spectrum from $BaSO_4$ according to the size of an area and line detectors.

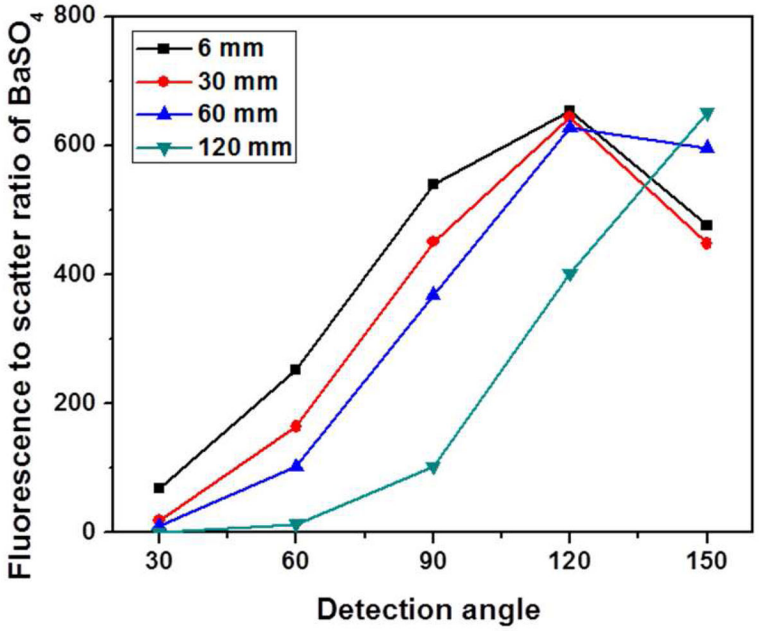

Figure 8.
The angular dependence of X-ray FSR for k_α from $BaSO_4$ with different diameters.

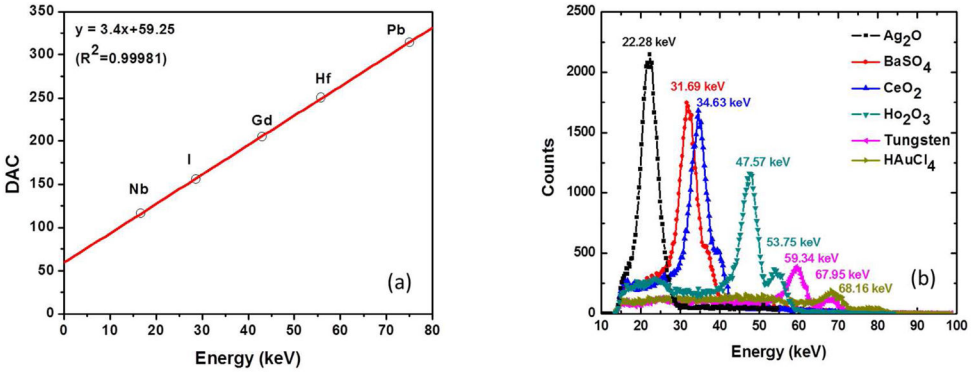

Figure 9.

(a) Linear correlation between the recorded pulse height at the peak centers and the known X-ray fluorescence energies of five fluorescent materials with CZT-based photon-counting detector. (b) Acquired six fluorescent material's spectra using CZT-based photon-counting detector after energy calibration. The recorded X-ray fluorescence energy of each material is included with each peak.

Table 1

Fluorescence energy of the fluorescent materials.

Target element	Material	K_α energy (keV)	K_β energy (keV)
Br	KBr	11.924	13.292
Nb	$NbCl_5$	16.615	18.623
Ag	Ag_2O	22.163	24.943
I	$C_{19}H_{26}I_3N_3O_9$ (Iohexol)	28.612	32.295
Ba	$BaSO_4$	32.194	36.378
Ce	CeO_2	34.720	39.258
Gd	$C_{16}H_{28}GdN_5O_9$ (Gadodiamide)	42.996	48.696
Ho	Ho_2O_3	47.547	53.878
Hf	HfO_2	55.790	63.236
W	W(powder)	59.318	67.244
Au	$HAuCl_4$	68.804	77.985
Pb	$Pb(NO_3)_2$	74.969	84.936
U	$UO_2(NO_3)_2$	98.440	111.303